

# LOW-MASS STAR FORMATION TRIGGERED BY EARLY SUPERNOVA EXPLOSIONS

GEN CHIAKI<sup>†1</sup>, NAOKI YOSHIDA<sup>†</sup> AND TETSU KITAYAMA<sup>‡</sup>

<sup>†</sup>Department of Physics, Graduate School of Science, University of Tokyo, 7-3-1 Hongo, Bunkyo, Tokyo 113-0033, Japan

<sup>‡</sup>Department of Physics, Toho University, Funabashi, Chiba 274-8510, Japan

*To Appear in ApJ*

## ABSTRACT

We study the formation of low-mass and extremely metal-poor stars in the early universe. Our study is motivated by the recent discovery of a low-mass ( $M_* \leq 0.8 M_\odot$ ) and extremely metal-poor ( $Z \leq 4.5 \times 10^{-5} Z_\odot$ ) star in the Galactic halo by Caffau et al. (2011). We propose a model that early supernova (SN) explosions trigger the formation of low-mass stars via shell fragmentation. We first perform one-dimensional hydrodynamic simulations of the evolution of an early SN remnant. We show that the shocked shell undergoes efficient radiative cooling and then becomes gravitationally unstable to fragment and collapse in about a million years. We then follow the thermal evolution of the collapsing fragments using a one-zone code. Our one-zone calculation treats chemistry and radiative cooling self-consistently in low-metallicity gas. The collapsing gas cloud evolves roughly isothermally, until it cools rapidly by dust continuum emission at the density  $10^{13}$ – $10^{14}$  cm<sup>-3</sup>. The cloud core then becomes unstable and fragments again. We argue that early SNe can trigger the formation of low-mass stars in the extremely metal-poor environment as Caffau et al. (2011) discovered recently.

*Subject headings:* stars: formation — supernovae: general

## 1. INTRODUCTION

Stars with masses  $M_* \lesssim 0.8 M_\odot$  formed in the early universe may survive to the present day. Such old low-mass stars should typically have very low metallicities because they were formed from a gas that had not been significantly enriched with heavy elements. They carry invaluable information on the early chemical evolution of the Galaxy (Beers & Christlieb 2005). Recently, Caffau et al. (2011) discovered a low-mass and extremely metal-deficient star in the halo of the Galaxy. The star has extremely small abundances of carbon and nitrogen. The upper limit of corresponding metallicity of the star is estimated to be  $4.5 \times 10^{-5} Z_\odot$  (Caffau et al. 2011). Furthermore, the ratio of the abundances of carbon and oxygen derived from the spectra of the star suggests that the parent cloud from which the star was born had been chemically enriched by core-collapse supernovae (Caffau et al. 2011).

It is generally thought that metal-free primordial stars are predominantly massive (*e.g.*, Bromm et al. 2009) although not extremely massive (Hosokawa et al. 2011). This is largely because metal-free gas lacks efficient coolants other than hydrogen molecules; a primordial gas cloud is thermally stable throughout its pre-stellar collapse (Omukai & Yoshii 2003; Yoshida et al. 2008). Theoretical studies suggest that a trace amount of heavy elements provide efficient cooling in low-metallicity gas, which may then enable the formation of low-mass stars (see Bromm & Yoshida 2011, for a review). There is another argument that the existence of dust grains in low-metallicity gas is crucial for the low-mass star formation (Schneider et al. 2003; Omukai et al. 2005, 2010). Although it is still unclear whether or not gas metallicity is the key quantity to determine the characteristic stellar mass, and whether or not there is “critical metallicity” for low-mass star formation, there must be a mechanism

for the formation of low-mass stars in extremely low-metallicity gas<sup>2</sup>.

SN explosions of the first generation stars are thought to have enriched the early universe with the first heavy elements. Three-dimensional simulations of early SN explosions are performed by, *e.g.*, Bromm et al. (2003) and Greif et al. (2010). These studies show heavy elements are effectively dispersed into the inter-galactic medium. Whalen et al. (2010) argue that ultraviolet radiation from a massive progenitor star modifies the density structure of the ambient gas before SN explosion. Overall, an early SN explosion can trigger the formation of low-mass and low-metallicity stars. Nagakura et al. (2009) study the evolution of SN remnants with metallicities of  $Z = 10^{-4}$  and  $10^{-2} Z_\odot$ . The SN shell becomes gravitationally unstable for a certain range of parameters such as explosion energy, ambient gas density, and metallicity. They show that the typical mass scale of the fragments is  $\sim 10^3$ – $10^4 M_\odot$  and argue that a low-mass star forms after the further evolution of the fragment. Machida et al. (2005) semi-analytically calculate the evolution of SN shells before and after the shell fragmentation in a primordial gas. They show that the Jeans mass of the fragment is below the solar mass when the fragment becomes optically thick. However, it remains uncertain whether the gas cloud further fragment or not.

In this paper, we study SN-triggered star formation, using hydrodynamic simulations. We first run one-dimensional hydrodynamic simulations to follow the thermal evolution of an early SN remnant. We here assume the ambient gas around the SN has nearly the primordial composition with a trace amount of heavy elements,  $Z = 1.0 \times 10^{-5} Z_\odot$  and  $4.5 \times 10^{-5} Z_\odot$ , presumably ejected by earlier generation stars. We determine whether or not the shocked SN shell is gravitationally

<sup>1</sup> E-mail: gen.chiaki@utap.phys.s.u-tokyo.ac.jp

<sup>2</sup> In this paper, we use the term “low-mass” for a mass less than  $1 M_\odot$

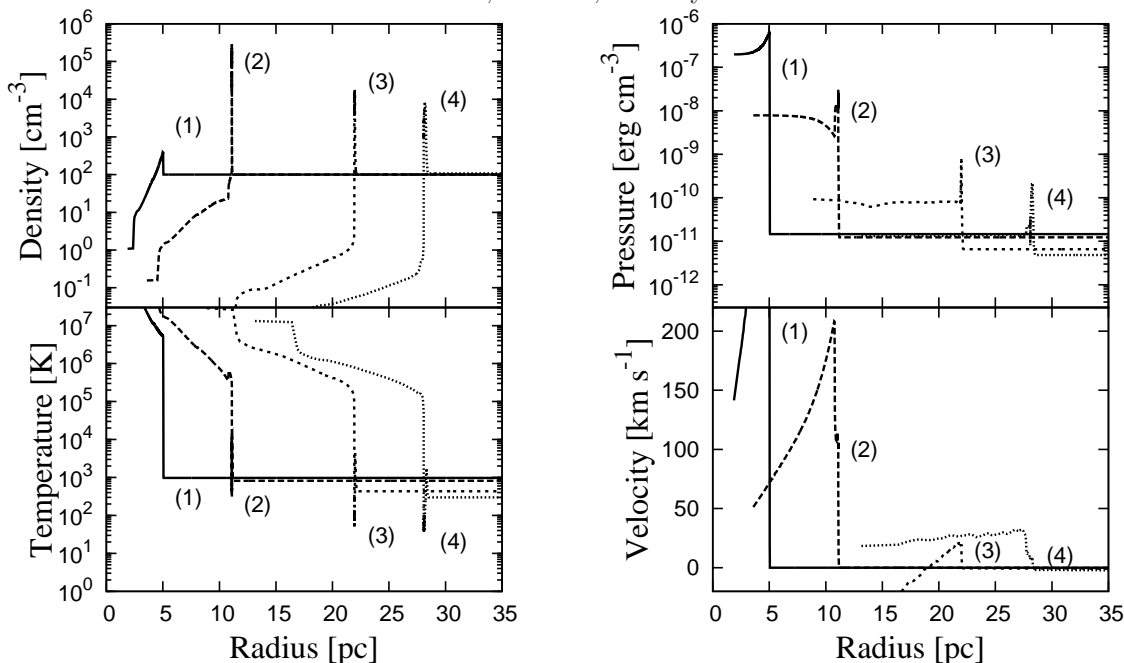


FIG. 1.— We plot the evolution of the density, temperature, pressure, and velocity profiles of the supernova remnant for  $(E_{\text{SN}}, n_0, Z) = (1 \times 10^{52} \text{ erg}, 100 \text{ cm}^{-3}, 1.0 \times 10^{-5} Z_{\odot})$  at the time (1)  $t = 3.2 \times 10^3$ , (2)  $3.2 \times 10^4$ , (3)  $3.2 \times 10^5$ , and (4)  $8.6 \times 10^5$  yr. The blast wave driven by SN explosion sweeps up the ambient medium and the SN-shocked shell is formed. Epoch (1) corresponds to the Sedov-Taylor phase, in which the shell expands adiabatically. Then, the cold dense shell forms by radiative cooling at epoch (2), and eventually the shell is decelerated sufficiently to be gravitationally unstable at epoch (4).

unstable to fragment by using linear analysis of density perturbations. We show that gravitational instability is triggered in the shell for a wide range of the supernova explosion energies,  $E_{\text{SN}} = 1 \times 10^{51} - 3 \times 10^{52} \text{ erg}$ , and for large ambient gas density,  $n_0 \geq 10 \text{ cm}^{-3}$ . Finally, we study the subsequent evolution of the collapsing fragments, using a one-zone code. While the gas cloud continues collapsing gravitationally, it cools rapidly by dust thermal emission and eventually fragments to sub-solar mass clumps.

## 2. NUMERICAL METHOD

### 2.1. Code

#### 2.1.1. Ante-fragmentation phase

We perform one-dimensional hydrodynamic calculations to follow the dynamics of an SN remnant until the shocked gas shell undergoes gravitational instability (hereafter, we call this phase *ante-fragmentation phase*). We use the code of Kitayama et al. (2004) and Kitayama & Yoshida (2005) which employs the second-order Lagrangian finite-difference scheme in spherically symmetric geometries. The basic equations are presented in §2 of Kitayama et al. (2004).

We implement the relevant radiative cooling processes to the hydrodynamical code as follows. In the high temperature regime ( $T > 10^4 \text{ K}$ ), assuming that the gas is in collisional ionization equilibrium, we adopt the cooling function of Sutherland & Dopita (1993). The cooling functions for  $Z < 10^{-3} Z_{\odot}$  are derived by interpolating the cooling functions for  $Z = 10^{-3} Z_{\odot}$  and  $Z = 0$ . The cooling rate due to inverse Compton scattering is also included.

In the lower temperature regime ( $T < 10^4 \text{ K}$ ), we solve the non-equilibrium chemical reactions and radiative processes of the following fifteen species:  $e^-$ , H,  $\text{H}^+$ ,  $\text{H}^-$ , D,  $\text{D}^+$ ,  $\text{D}^-$ , He,  $\text{He}^+$ ,  $\text{He}^-$ ,  $\text{H}_2$ ,  $\text{H}_2^+$ , HD,  $\text{HD}^+$ ,

and  $\text{HeH}^+$ . The molecular cooling rates are taken from Galli & Palla (1998) for  $\text{H}_2$ , Lipovka et al. (2005) and from Flower et al. (2000) for HD. We also calculate the fine-structure transition line cooling of heavy elements including C, O, Si, and Fe. These species are assumed to be in the form of C II, O I, Si II, and Fe II, respectively. The fraction of each species in the gas is derived by multiplying the solar abundance by metallicity ( $Z/Z_{\odot}$ ). The solar abundances of C, O, Si, and Fe relative to hydrogen are  $2.45 \times 10^{-4}$ ,  $4.90 \times 10^{-4}$ ,  $3.63 \times 10^{-5}$ , and  $3.16 \times 10^{-5}$ , respectively (Santoro & Shull 2006) throughout the one-dimensional calculation. Also, the atomic level transition rates are taken from Santoro & Shull (2006).

#### 2.1.2. Postfragmentation phase

After the supernova shell becomes gravitationally unstable (see §3.2 below), fragments in a shell are expected to collapse further to trigger star formation. We perform one-zone calculations to follow the thermal and chemical evolution of one of such collapsing gas clouds. We assume that the collapse occurs approximately in a spherically symmetric manner. Then, the time evolution of the gas density,  $\rho$ , is described as

$$\frac{d\rho}{dt} = \frac{\rho}{t_{\text{ff}}}. \quad (1)$$

In this equation,  $t_{\text{ff}}$  denotes the free-fall time as

$$t_{\text{ff}} = \left( \frac{3\pi}{32G\rho} \right)^{1/2}, \quad (2)$$

where  $G$  is the Newtonian gravitational constant. The evolution of specific internal energy,  $e$ , is

$$\frac{de}{dt} = -p \frac{d}{dt} \left( \frac{1}{\rho} \right) + \frac{\Gamma - \Lambda}{\rho}, \quad (3)$$

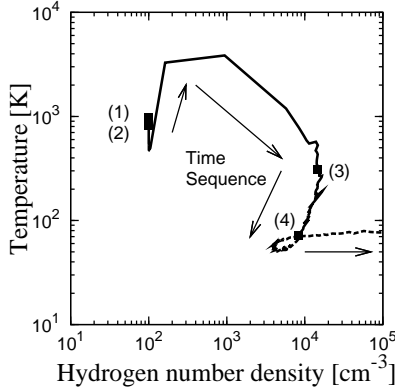


FIG. 2.— We plot the evolution of the density and temperature of a fluid element, which is initially located at 20.8 pc from the center. Here, the result for the SN model of  $(E_{\text{SN}}, n_0, Z) = (1 \times 10^{52} \text{ erg}, 100 \text{ cm}^{-3}, 1.0 \times 10^{-5} Z_{\odot})$  is shown. Solid and dashed curves denote the evolution before and after fragmentation, respectively. Both results are obtained by our one-dimensional calculations. Points (1) to (4) indicate the epochs in Figure 1. After epoch (4), the density in the region turns to increase by self-gravity.

where  $p$  denotes the pressure and  $\Gamma$  and  $\Lambda$  denote heating and cooling rate per unit volume, respectively. The temperature of the cloud,  $T$ , is related to the internal energy as

$$e = \frac{1}{\gamma - 1} \frac{kT}{\mu m_{\text{H}}}, \quad (4)$$

where  $\mu$  is the mean molecular weight,  $m_{\text{H}}$  is the mass of hydrogen nuclei. In equation (4),  $\gamma$  is the adiabatic index which is calculated by taking average over all species as *e.g.*, Omukai & Nishi (1998).

In our one-zone model, the low-metallicity gas is assumed to consist of the following chemical species:  $e^-$ ,  $\text{H}$ ,  $\text{H}^+$ ,  $\text{H}^-$ ,  $\text{D}$ ,  $\text{D}^+$ ,  $\text{D}^-$ ,  $\text{He}$ ,  $\text{He}^+$ ,  $\text{He}^-$ ,  $\text{C}$ ,  $\text{C}^+$ ,  $\text{O}$ ,  $\text{O}^+$ ,  $\text{H}_2$ ,  $\text{H}_2^+$ ,  $\text{H}_2^-$ ,  $\text{HD}$ ,  $\text{HD}^+$ ,  $\text{HD}^-$ ,  $\text{OH}$ ,  $\text{H}_2\text{O}$ ,  $\text{H}_2\text{O}^+$ ,  $\text{O}_2$ ,  $\text{O}_2^+$ ,  $\text{CO}$ ,  $\text{CO}^+$ ,  $\text{CO}_2$ , and  $\text{CO}_2^+$ . We assume that 72 % of carbon and 46 % of oxygen are condensed to dust grains as in the local interstellar matter (Pollack et al. 1994). We include atomic cooling by C II and O I but neglect the contributions from less abundant Si II and Fe II because these species do not have effect on the thermal evolution of the gas cloud (Schneider et al. 2012). The adiabatic compressional heating and the chemical heating by  $\text{H}_2$  formation are the dominant heating processes. We also consider the dust cooling in the calculations. The reaction rates and corresponding cooling rates are taken from Omukai et al. (2005, 2010). We use the Sobolev length approximation for optically thick cooling as in Omukai (2000) and Yoshida et al. (2006).

## 2.2. Initial Conditions

We set metallicities of the circumstellar medium  $Z = 1.0 \times 10^{-5} Z_{\odot}$  conservatively and  $4.5 \times 10^{-5} Z_{\odot}$ , the upper bound of the metallicity of the star Caffau et al. (2011) observed. We assume that the progenitor star is hosted by an early small dark matter halo with mass  $M_{\text{h}} = 10^6 M_{\odot}$  at a redshift of  $z = 20$  (Yoshida et al. 2003). The gravitational potential of the dark matter is fixed as in Kitayama & Yoshida (2005). We work with the  $\Lambda$ CDM model with the matter density  $\Omega_{\text{m}} = 0.27$ , the baryon density  $\Omega_{\text{b}} = 0.045$ , the cosmological constant  $\Omega_{\Lambda} = 0.73$ , the Hubble constant  $h = 0.71$ , in units of  $100 \text{ km s}^{-1} \text{ Mpc}^{-1}$ , and the absolute density fluctuation

$\sigma_8 = 0.80$  consistent with WMAP 7 data (Larson et al. 2011).

The density of the circumstellar medium at the time when SN explosions occur depends on a number of factors such as the mass of the hosting halo (Whalen et al. 2004, 2008; Kitayama et al. 2004) and the ultraviolet luminosity of the progenitor star (Shu et al. 2002; Alvarez et al. 2006). Thus, for simplicity, we assume that the surrounding gas density is initially uniform for our one-dimensional hydrodynamic simulations and the initial density is set  $n_0 = 1, 10, 100$ , and  $1000 \text{ cm}^{-3}$ .

We assume that the surrounding gas with primordial composition is pre-enriched with a trace amount of heavy elements. Thus, through this paper, the hydrogen mass fraction is  $X = 0.74$ , the helium mass fraction is  $Y = 0.26$  (Aver et al. 2010), and the deuterium number fraction is  $\text{D}/\text{H} = 2.9 \times 10^{-5}$  (Iocco et al. 2009). We set the initial gas temperature  $T = 10^3 \text{ K}$ , and initial ionization fraction of hydrogen is uniformly  $10^{-4}$ . The fraction of hydrogen molecule is  $10^{-3}$  at the beginning<sup>3</sup>. The radial velocity is set  $v = 0 \text{ km s}^{-1}$ . We test three explosion energies,  $E_{\text{SN}} = 1 \times 10^{51}$ ,  $1 \times 10^{52}$ , and  $3 \times 10^{52} \text{ erg}$ . We assume a point-source explosion and at the time  $t = 0$ , the corresponding thermal energy is deposited in the innermost cell.

## 3. RESULTS

### 3.1. Shell Evolution

#### 3.1.1. Larger ambient gas density

Figure 1 shows the structures of the shell for  $(E_{\text{SN}}, n_0, Z) = (1 \times 10^{52} \text{ erg}, 100 \text{ cm}^{-3}, 1.0 \times 10^{-5} Z_{\odot})$  at the time (1)  $t = 3.2 \times 10^3$ , (2)  $3.2 \times 10^4$ , (3)  $3.2 \times 10^5$ , and (4)  $8.6 \times 10^5 \text{ yr}$ . Figure 2 illustrates the evolution of the gas density and temperature for a fluid element that is densest when the shell becomes gravitationally unstable and that is initially located at 20.8 pc from the center. The evolution of the SN shell structure is described as follows. In the initial Sedov-Taylor phase, the SN remnant expands adiabatically as long as the radiative cooling time,  $t_{\text{cool}} = \rho e / \Lambda$ , is longer than the shell expansion time scale,  $t_{\text{exp}} = R / V$  (Sedov 1958). Then, radiative cooling becomes effective and the gas just behind the shock starts to lose its thermal energy. At  $t \simeq 2 \times 10^4 \text{ yr}$  after the SN explosion, the cold shell is pushed by the large pressure of the inner hot gas, forming a very dense shell (the pressure-driven snowplough phase). During the pressure-driven phase, the fluid element plotted in Figure 2 enters the shock front, increasing its density and temperature rapidly. The inner hot region still impacts the cold shell, generating multiple weak shocks behind the shell. We see this as oscillatory features from epoch (3) to epoch (4) in Figure 2. Finally, at epoch (4), the shell is decelerated sufficiently to be gravitationally unstable as we shall discuss in §3.2.

#### 3.1.2. Smaller ambient gas density

<sup>3</sup> The structure and evolution of SN shells are indeed insensitive to the circumstellar temperature and chemical compositions because the upstream pressure is negligible against the downstream pressure at the beginning of the shell evolution. We also confirm that at the end of simulations the upstream temperature becomes below  $10^3 \text{ K}$  by radiative cooling even if we start the simulation with the temperature of  $10^4 \text{ K}$ .

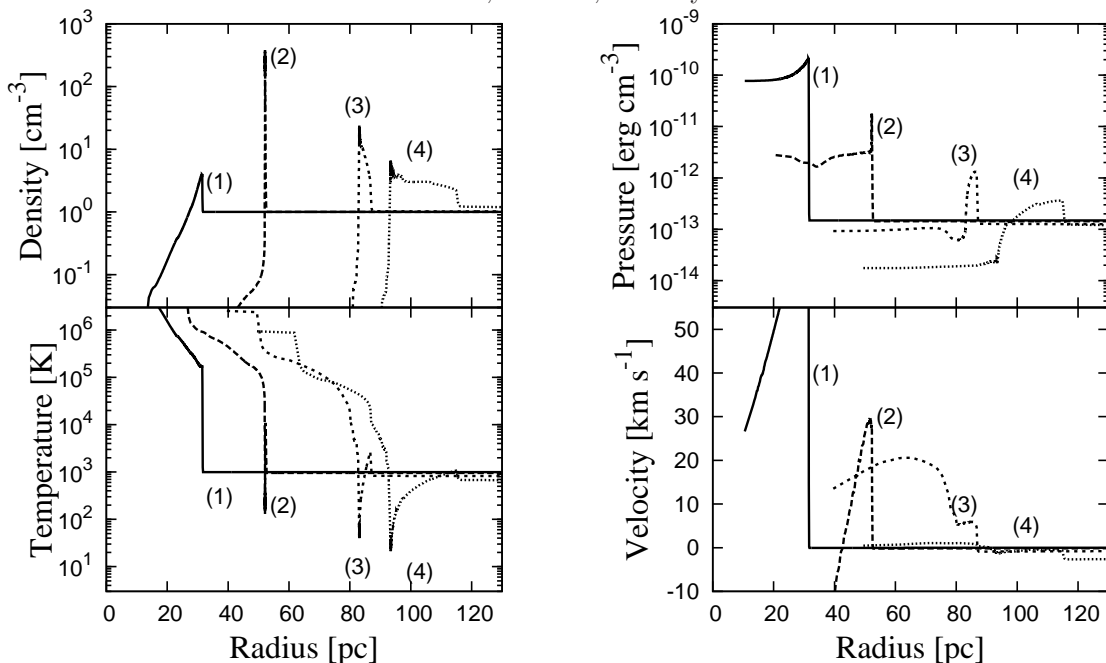


FIG. 3.— Same as Figure 1, but for  $(E_{\text{SN}}, n_0, Z) = (1 \times 10^{51} \text{ erg}, 1 \text{ cm}^{-3}, 1.0 \times 10^{-5} Z_{\odot})$  at the time (1)  $t = 1.0 \times 10^5$ , (2)  $5.6 \times 10^5$ , (3)  $3.2 \times 10^6$ , and (4)  $1.0 \times 10^7$  yr.

Figure 3 shows the structures of the shell for  $(E_{\text{SN}}, n_0, Z) = (1 \times 10^{51} \text{ erg}, 1 \text{ cm}^{-3}, 1.0 \times 10^{-5} Z_{\odot})$  at the time (1)  $t = 1.0 \times 10^5$ , (2)  $5.6 \times 10^5$ , (3)  $3.2 \times 10^6$ , and (4)  $1.0 \times 10^7$  yr. Figure 4 illustrates the evolution of the gas density and temperature for a fluid element initially located at 34.3 pc from the center. In this model, the shell is in the Sedov-Taylor phase around epoch (1) and then enters the pressure-driven snowplough phase at  $t \simeq 2 \times 10^5$  yr. In this case with low ambient gas density, the transition from the Sedov-Taylor phase to the pressure-driven phase occurs later than the model with high ambient gas density. When the shell sweeps up denser ambient medium, radiative cooling of the shell, which is generally proportional to the square of gas density, becomes larger, and the enhanced radiative cooling makes the shell evolve faster. The shell continues to expand even after the pressure inside the shell declines due to radiative cooling, conserving the momentum (the momentum-conserving snowplough phase). In our calculation, the shell enters the momentum-conserving phase by epoch (3). The shell thickness increases because of the pressure in the shell. The internal energy of the shell remains higher by less effective radiative cooling. Around epoch (4), the elapsed time reaches the dynamical timescale for the dark matter halo hosting the progenitor star ( $t_{\text{dyn}} \sim 10^7$  yr for  $10^6 M_{\odot}$  halo at  $z \sim 20$ ).

### 3.2. Shell Fragmentation

#### 3.2.1. Criteria for fragmentation

There are several criteria proposed for the instability of an expanding and decelerating gas shell. Elmegreen (1994) derive approximate conditions for the collapse of an expanding and decelerating shell by linear analysis of density perturbations under the thin-shell approximation. Then, Iwasaki & Tsuribe (2008) and Iwasaki et al. (2011a,b) include the effect of the internal structure of the shell to the result by Elmegreen (1994). For a shell with average column density over the all solid angle,  $\Sigma_0$ ,

shell radius,  $R$ , and velocity  $V$ , the angular wavenumber of the perturbations that grow most rapidly is

$$\eta_{\text{peak}} = \frac{\pi G \Sigma_0}{c_{\text{eff}}^2} R, \quad (5)$$

and the growth rate of the perturbations with wavenumber  $\eta_{\text{peak}}$  is

$$\omega_{\text{peak}} = -\frac{3V}{R} + \left[ \left( \frac{V}{R} \right)^2 + \left( \frac{\pi G \Sigma_0}{c_{\text{eff}}} \right)^2 \right]^{1/2}. \quad (6)$$

In equations (5) and (6),  $c_{\text{eff}}$  is the effective sound speed as

$$c_{\text{eff}} = \left[ A \frac{2\pi G \Sigma_0^2}{\rho_{\text{max}}} + \left( \frac{c_T}{2} \right)^2 \right]^{1/2}, \quad (7)$$

where  $\rho_{\text{max}}$  is the peak density in the shell and  $c_T = (kT/\mu m_{\text{H}})^{1/2}$  is the sound speed for an isothermal shell with temperature  $T$ . The numerical factor  $A$  is determined as 0.39 by the detailed linear analysis for a shell with its outer boundary defined by the shock front and with its inner boundary defined by the stellar wind from a central star (Iwasaki et al. 2011a,b). Note that replacing  $c_{\text{eff}}$  with  $c_T$  and  $\Sigma_0$  with  $\rho_0 R/3$ , where  $\rho_0$  is the average pre-shell mass density, in equations (5) and (6) recovers the result of Elmegreen (1994).

In equation (6), the first and second terms in the right hand side represent the effect of the shell expansion and the last term represents the effect of the shell internal pressure and self-gravity. If the peak growth rate,  $\omega_{\text{peak}}$ , is positive, perturbations with the corresponding wavenumber have a growing solution, which means the SN-driven shell becomes gravitationally unstable and fragments with scales corresponding to  $\eta_{\text{peak}}$  start to grow in the shell. It is obvious that fast expansion (large  $V$ ) tends to smooth out perturbations. For the gas to become gravitationally unstable, its expansion



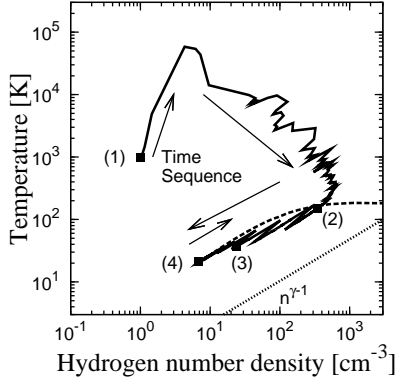


FIG. 4.— Same as Figure 2, but for  $(E_{\text{SN}}, n_0, Z) = (1 \times 10^{51} \text{ erg}, 1 \text{ cm}^{-3}, 1.0 \times 10^{-5} Z_{\odot})$ . Points (1) to (4) indicate the epochs in Figure 3. Dotted line shows an adiabatic trajectory,  $T \propto n^{\gamma-1}$ . The trajectory is along an adiabatic line between epochs (2) and (4) because the shell expands radially for small external pressure, while in larger ambient density case, the density declines slowly because the shell expansion is suppressed by the large external pressure and the temperature decreases by radiative cooling (Figure 2).

velocity must be sufficiently small such that

$$\frac{V}{R} < \frac{\pi G \Sigma_0}{\sqrt{8} c_{\text{eff}}}. \quad (8)$$

### 3.2.2. Application of the criterion to our results

In this section, we discuss whether the gravitational instability can be triggered or not. We apply the criterion by Iwasaki et al. (2011a,b) to our calculations because the internal structure of a shell is taken into account in their analysis<sup>4</sup>. In order to investigate the stability of the shell, we calculate the time evolution of the peak growth rate,  $\omega_{\text{peak}}$  [equation (6)] by using the radius of the shock front, the shock velocity, volume-weighted mean density, mass-weighted mean temperature, and mean molecular weight in the shell. In the snowplough phase, the shell is defined by the outer boundary (shock front) and the inner boundary. The outer boundary is determined as position where the density is  $1.1 \rho_0$ . The displacement of the inner boundary is defined as the point where density recovers the pre-shell density,  $\rho_0$ , inside the shock radius.

After the shell becomes gravitationally unstable, the shell is assumed to be separated into fragments. If the time for fragmentation is comparable to or larger than the dynamical timescale of the hosting halo,  $t_{\text{dyn}}$ , we do not count such cases as successful fragmentation of the SN shell in the cosmological context. After the dynamical timescale, it is likely that the halo itself collapses or is incorporated into a large halo, thereby the structure of the entire system would be much different.

Applying the fragmentation condition, we find that for the SN model of  $(E_{\text{SN}}, n_0, Z) = (1 \times 10^{52} \text{ erg}, 100 \text{ cm}^{-3}, 1.0 \times 10^{-5} Z_{\odot})$ , the compressed and decelerated shell becomes gravitationally unstable at

<sup>4</sup> Iwasaki et al. (2011a,b) presented the linear analysis for a shell defined by a shock front and an inner boundary formed by the pressure of the inner region. It is thus more appropriate to our results of the SN-driven shell defined by the shock front and the inner boundary although the shell inner boundary in the study of Iwasaki et al. (2011a,b) is driven by the pressure of the stellar wind from the central star. We have also checked that the result is qualitatively unchanged if we apply the result by Elmegreen (1994) which ignores the effect of the shell structure.

$t_{\text{inst}} = 8.3 \times 10^5 \text{ yr}$ . By contrast, for  $(E_{\text{SN}}, n_0, Z) = (1 \times 10^{51} \text{ erg}, 1 \text{ cm}^{-3}, 1.0 \times 10^{-5} Z_{\odot})$ , the peak growth rate  $\omega_{\text{peak}}$  becomes positive at  $t_{\text{inst}} = 1.0 \times 10^7 \text{ yr}$  when the shell is about to fall back ( $V \simeq 0$ ) by the gravitational potential of the host halo. In this model, since the time  $t_{\text{inst}}$  is comparable to the dynamical timescale, it is uncertain whether the shell fragments or collapses into the center of the halo.

Table 1 shows the physical properties of the shell at the time  $t_{\text{inst}}$  for SN models we study. The results are shown only for  $Z = 1.0 \times 10^{-5} Z_{\odot}$  because they are almost exactly the same as the results of the  $Z = 4.5 \times 10^{-5} Z_{\odot}$  models. It is because the fine-structure cooling of metals such as C and O has little effect on the evolution of the SN remnant in such an extremely metal-poor regime until the shell becomes gravitationally unstable. Also, the time  $t_{\text{inst}}$  is insensitive to the SN explosion energy. For a radiative remnant, the shock radius increases only as  $R \propto E_{\text{SN}}^{1/7}$  in the pressure-driven phase (Ostriker & McKee 1988). The time  $t_{\text{inst}}$  depends on the ambient gas density. As the ambient gas density is larger, denser and colder shell is formed as we discuss in §3.1.2 and the growth rate of the perturbations on the shell,  $\omega_{\text{peak}}$  becomes positive earlier. The Jeans mass (typical mass) of the fragment is shown in the last column of Table 1. The mass decreases as ambient gas density increases because the density of the shell swept up by the blast wave becomes larger.

Figure 5 shows the results of all the models that we investigated in a  $(E_{\text{SN}}, n_0)$  plane. These results are essentially the same for the respective model with  $4.5 \times 10^{-5} Z_{\odot}$ . The circles indicate models where both our criteria are met. For models with ambient density  $n_0 = 1 \text{ cm}^{-3}$ , the time for the gravitational instability,  $t_{\text{inst}}$ , is comparable to  $t_{\text{dyn}}$ . These models are marked by triangles. We cannot determine from our 1D calculations whether the shell fragments before the host halo evolves significantly. It would be needed to run a cosmological simulation that incorporate the hierarchical growth of dark halos, in order to follow the evolution of such systems properly.

### 3.3. Evolution of Fragments

We investigate the subsequent evolution of the fragment for the models with large ambient gas density  $n_0 > 10 \text{ cm}^{-3}$  where the SN-driven shell becomes gravitationally unstable well before  $10^7 \text{ yr}$ . In these models, the time,  $t_{\text{inst}}$  when SN shells fragment is comparable to the free-fall timescale,  $t_{\text{ff}}$ , of the shell at the time  $t_{\text{inst}}$ . The fragments are expected to contract gravitationally on the free-fall time scale (equation 1). Curves in Figure 6 denote the evolutionary trajectories of the core of each fragment calculated by our one-zone code for the metallicities  $1.0 \times 10^{-5} Z_{\odot}$  and  $4.5 \times 10^{-5} Z_{\odot}$  when SN explosion energy and ambient density are  $(E_{\text{SN}}, n_0) = (1 \times 10^{52} \text{ erg}, 100 \text{ cm}^{-3})$ . The initial density, temperature and the chemical species' abundances are taken from the result of our one-dimensional calculation. We use the result at the time when the gravitational instability is triggered in the shell.

The temperature stays between a few hundred to one thousand Kelvins while the density increases over many orders of magnitudes. The compressional heating is

TABLE 1  
PROPERTIES OF FRAGMENTS ( $Z = 1.0 \times 10^{-5} Z_{\odot}$ )

$n_0$ ( $\text{cm}^{-3}$ )	$E_{\text{SN}}$ ( $10^{51}$ erg)	$t_{\text{inst}}$ (Myr)	$n_{\text{H}}$ ( $\text{cm}^{-3}$ )	$T$ (K)	$R$ (pc)	$\Delta R$ (pc)	$\eta_{\text{peak}}$	$M_{\text{shell}}$ ( $M_{\odot}$ )	$M_{\text{Jeans}}$ ( $M_{\odot}$ )
1	1.0	10.23	2.9E+00	568.6	115.9	22.84	3.0	3.0E+05	4.8E+05
	10.0	10.84	6.7E+00	466.8	196.6	12.89	8.7	1.3E+06	2.4E+05
	30.0	10.35	1.1E+01	419.7	250.9	9.17	14.4	2.6E+06	1.6E+05
10	1.0	3.39	5.9E+01	300.2	45.6	3.53	6.9	1.7E+05	4.1E+04
	10.0	2.99	1.7E+02	239.8	75.2	1.72	21.5	6.7E+05	1.7E+04
	30.0	2.63	2.4E+02	215.2	93.9	1.42	36.5	1.3E+06	1.2E+04
100	1.0	1.06	1.1E+03	191.6	17.9	0.68	14.2	9.3E+04	4.9E+03
	10.0	0.83	2.4E+03	182.8	28.5	0.43	38.5	3.5E+05	3.0E+03
	30.0	0.72	3.8E+03	186.4	35.2	0.33	58.4	6.4E+05	2.5E+03
1000	1.0	0.32	1.4E+04	202.5	6.9	0.19	19.5	5.1E+04	1.5E+03
	10.0	0.25	3.1E+04	206.5	10.7	0.12	48.8	1.8E+05	1.0E+03
	30.0	0.22	4.0E+04	223.0	13.2	0.12	69.8	3.4E+05	1.0E+03

NOTE. —  $Z$ : metallicity of the ambient material,  $n_0$ : ambient gas density,  $E_{\text{SN}}$ : explosion energy,  $t_{\text{inst}}$ : time when the gravitational instability first appears,  $n_{\text{H}}$ : volume-averaged Hydrogen number density in the shell,  $T$ : mass-weighted average of temperature in the shell,  $R$ : radius of the shock front,  $\Delta R$ : shell thickness,  $\eta_{\text{peak}}$ : peak wavenumber of the perturbations,  $M_{\text{shell}}$ : mass of the shell, and  $M_{\text{Jeans}}$ : Jeans mass, at  $t = t_{\text{inst}}$

largely balanced by radiative cooling until the Hydrogen atomic number density increases to  $n_{\text{H}} \sim 10^{16} \text{ cm}^{-3}$ . There are, however, two slight declines as clearly seen in Figure 6. The first decline appears at  $n_{\text{H}} \sim 10^4 \text{ cm}^{-3}$  where cooling by HD molecular lines is efficient. The second decline appears at  $n_{\text{H}} \sim 10^{13} \text{ cm}^{-3}$  where cooling by dust thermal emission is efficient. In the latter regime, the gas cloud core becomes further unstable and is likely to fragment into multiple clumps (Omukai et al. 2005).

The gravitational instabilities occur when the dust cooling timescale is shorter than the free-fall timescale. The gas cooling by dust is due to heat transfer from gas particles to cold dust grains (see Stahler & Palla 2005, §7.4.3). Then, essentially the gas pressure determines the juncture for efficient dust cooling as

$$p = n_{\text{H}} k T > \frac{32G}{9\pi} \left( \frac{a_d \rho_d}{Z_d \alpha} \right)^2, \quad (9)$$

where  $a_d$  and  $\rho_d$  denote the mean radius and mass density of an individual dust grain,  $Z_d$  is dust mass fraction, and  $\alpha$  is the accommodation coefficient for heat transfer between gas and dust. From the typical values of  $a_d \sim 10^{-5} \text{ cm}$ ,  $\rho_d \simeq 3 \text{ g cm}^{-3}$  (Love et al. 1994),  $Z_d \sim 10^{-2}(Z/Z_{\odot})$ , and  $\alpha \sim 0.1$ , the region on the  $n$ - $T$  plane where dust cooling becomes efficient is

$$\frac{p}{k} = n_{\text{H}} T \gtrsim 4.9 \times 10^{15} \text{ cm}^{-3} \text{ K} \left( \frac{Z/Z_{\odot}}{10^{-5}} \right)^{-2}. \quad (10)$$

The triangles in Figure 6 denotes the points where the gas clouds satisfy the condition given by equation (10). The corresponding Jeans mass at the point is  $0.4 M_{\odot}$  for  $Z = 1.0 \times 10^{-5} Z_{\odot}$  and  $3 M_{\odot}$  for  $4.5 \times 10^{-5} Z_{\odot}$ . The Jeans mass further decreases as the gas temperature rapidly decreases by dust cooling, as can be seen in Figure 6.

The rapid dust cooling causes deformation of the cloud core into a filamentary structure. Tsuribe & Omukai (2008) show, using three-dimensional simulations, that an initially perturbed gas cloud is significantly elongated to filamentary shape and further fragments into small pieces when dust cooling operates for the metallicities  $10^{-6} \lesssim Z/Z_{\odot} \lesssim 10^{-5}$ . The deformation instability occurs when the deformation parameter, defined as the effective ratio of specific heats,  $\gamma_{\text{eff}} \equiv$

$d \log p / d \log \rho$ , is less than a critical value  $\gamma_{\text{crit}} = 1.097$  (Hanawa & Matsumoto 2000; Lai 2000). In our calculations,  $\gamma_{\text{eff}}$  declines rapidly below the critical value when the dust cooling becomes efficient. The deformation parameter is 0.5 at a minimum when  $n_{\text{H}} \sim 10^{13} \text{ cm}^{-3}$  for  $Z = 1.0 \times 10^{-5} Z_{\odot}$ . The value is common with all explosion energies we set. For  $Z = 4.5 \times 10^{-5} Z_{\odot}$ , the minimum value of  $\gamma_{\text{eff}}$  is 0.3–0.4 at  $n_{\text{H}} \sim 10^{12} \text{ cm}^{-3}$ . The contracting gas clouds are strongly unstable to deformation in these regimes.

When the instability occurs, regardless of the SN explosion energies and metallicities, the Jeans mass is  $0.01$ – $0.1 M_{\odot}$  which is the characteristic mass of a fragment (protostar). The ambient gas quickly accretes onto the protostars and their mass likely become larger (Larson 1969). However, the subsequent evolution of the protostars will be highly dynamical. According to Portegies Zwart et al. (2010), some of the protostars can attain velocities above the escape velocity of the parent gas cloud through dynamical interactions among them. They would then escape from the gas cloud before the protostars become massive. One natural outcome would then be the formation of low-mass stars.

#### 4. DISCUSSION

We have studied the evolution of an early SN remnant with a metallicity of  $\sim 10^{-5} Z_{\odot}$ . The supernova shell satisfies the criterion for gravitational instability at  $t \simeq 10^5$ – $10^6$  yr, to form multiple fragments with the characteristic Jeans mass of  $M_{\text{Jeans}} \sim 10^3$ – $10^4 M_{\odot}$  for a wide range of the SN explosion energies,  $E_{\text{SN}} = 1 \times 10^{51}$ – $3 \times 10^{52}$  erg, and large ambient gas density,  $n_0 \gtrsim 10 \text{ cm}^{-3}$ . We have then followed the thermal evolution of one of the fragments using one-zone calculations. The gas cloud core evolves roughly isothermally until the density increases to  $n_{\text{H}} \sim 10^{13} \text{ cm}^{-3}$ , where efficient cooling by dust thermal emission brings the gas temperature from  $\sim 10^3$  K to  $\sim 300$  K rapidly. The unstable core is expected to deform and fragment again into multiple clumps (protostars) with masses of  $\sim 0.01$ – $0.1 M_{\odot}$  regardless the SN explosion energies and metallicities. If some of the protostars escape from the host gas cloud before growing in mass over  $\sim 0.8 M_{\odot}$ , they would live long to the present day. We argue that the shell fragmentation of an

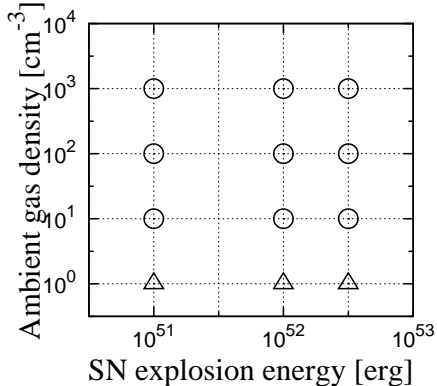


FIG. 5.— Fragmentation conditions for each our SN model. The result is common between the model with  $Z = 1.0 \times 10^{-5} Z_{\odot}$  and  $4.5 \times 10^{-5} Z_{\odot}$ . The circles indicate models where fragmentation condition is met. The triangles indicate models for which it is uncertain by our calculations whether the shell fragments or not (see text).

early SN remnant is a viable scenario for the formation of low-mass and extremely low-metallicity stars.

There have been several theoretical studies which suggest the formation of low-mass stars in low-metallicity gas using numerical simulations. For metallicities of  $\sim 10^{-5} Z_{\odot}$ , small mass clumps are formed from a rotating gas cloud (Tsuribe & Omukai 2008) and in turbulent gas (Dopcke et al. 2011) in many conditions these authors examined. Our hydrodynamic calculations are based on SN explosions of an early generation of stars. The end point of the hydrodynamic simulation of the SN remnant, when the shocked shell becomes gravitationally unstable, provides physically motivated initial conditions for our one-zone calculations. Therefore, we are able to propose, for the first time, a consistent model of how low-metallicity stars are formed in the early universe.

We note that there are still limitations in the one-dimensional and one-zone simulations. Non-spherical structures of an SN remnant might have substantial effects on the shell fragmentation. Chevalier & Theys (1975) and Chevalier & Imamura (1982) show that shell instabilities might enhance density perturbations around an SN remnant to form dense clumps in early epochs of the remnant evolution. Dense gas clumps could form even earlier than we have shown in this paper. Clearly, full three-dimensional calculations are needed to study in detail the evolution of an SN shell. Our calculations may provide basic configurations for such studies on the formation of low-mass stars in low-metallicity gas.

Currently standard models of galaxy formation are based on the hierarchical growth of cold dark matter halos. Recent high-resolution  $N$ -body simulations show that tens of thousands of early small halos assemble a Milky Way size halo (Gao et al. 2010; Wang et al. 2011). Although stars formed in the earliest halos are likely populated in the central bulge region, there should be a substantial fraction of the remnants of early halos orbiting

in the halo of the Galaxy (Tumlinson 2010; Gao et al. 2010). Caffau et al. (2011) may have found one of such “fossils”. Future surveys of metal-poor stars will provide the relative number fraction of extremely metal-poor stars, which will then constrain the overall formation efficiency of low-mass stars in the scenario we propose here.

The authors thank K. Omukai, M. N. Machida, K. Iwasaki, T. Tsuribe, and colleagues at IPMU for fruitful discussions and helpful advice. We are grateful to an anonymous referee of ApJ, who suggested us to derive the metallicity dependence of the critical pressure for the dust cooling. Part of the simulations were performed at the Center for Computational Astrophysics at the National Astronomical Observatory of Japan. This work is supported in part by the Grants-in-Aid for Young Scientists (S: 20674003, B: 21740139) by the Japan Society for the Promotion of Science. N.Y. acknowledges financial support from World Premier International Research Center Initiative (WPI Initiative), MEXT, Japan.

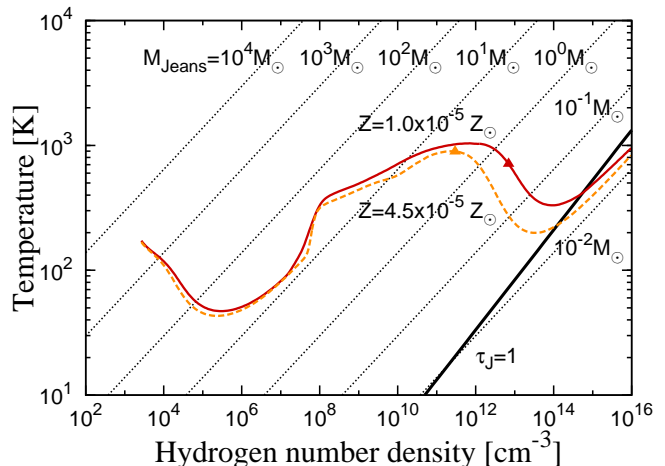


FIG. 6.— We plot the thermal evolution of the core of a collapsing fragment for  $(E_{\text{SN}}, n_0) = (1 \times 10^{52} \text{ erg}, 100 \text{ cm}^{-3})$ . Red and orange curves denote the trajectories for  $Z = 1.0 \times 10^{-5} Z_{\odot}$  and  $4.5 \times 10^{-5} Z_{\odot}$ , respectively. The initial condition of the one-zone calculation is determined using the result of our one-dimensional calculation. The initial density and temperature are set as the averaged values over the shell at the time when the shell fragments. Triangles are plotted at the points where the rapid dust cooling becomes dominant [equation (10) is satisfied] for each metallicity. Thick solid line indicates the opacity limit characterized by  $\tau_J = 1$ , where the cloud core is optically thick to continuum radiation (see e.g. Omukai 2000). The instability that induces deformation of the fragment occurs when the temperature decreases by rapid cooling ( $\gamma_{\text{eff}} \lesssim 1$ ). The fragment continues to deform, inducing further fragmentation until the temperature stops to decrease. The corresponding Jeans mass at the point is  $0.01\text{--}0.1 M_{\odot}$  which is regarded as the characteristic mass of a protostar.

## REFERENCES

- Alvarez, M. A., Bromm, V., & Shapiro, P. R. 2006, ApJ, 639, 621  
Aver, E., Olive, K. A., & Skillman, E. D. 2010, J. Cosmology Astropart. Phys., 5, 3  
Beers, T. C., & Christlieb, N. 2005, ARA&A, 43, 531  
Bromm, V., Yoshida, N., & Hernquist, L. 2003, ApJ, 596, L135  
Bromm, V., Yoshida, N., Hernquist, L., & McKee, C. F. 2009, Nature, 459, 49  
Bromm, V., & Yoshida, N. 2011, ARA&A, 49, 373  
Caffau, E., Bonifacio, P., François, P., et al. 2011, Nature, 477, 67  
Chevalier, R. A., & Theys, J. C. 1975, ApJ, 195, 53  
Chevalier, R. A., & Imamura, J. N. 1982, ApJ, 261, 543

- Dopcke, G., Glover, S. C. O., Clark, P. C., & Klessen, R. S. 2011, *ApJ*, 729, L3
- Elmegreen, B. G. 1994, *ApJ*, 427, 384
- Flower, D. R., Le Bourlot, J., Pineau des Forets, G., & Roueff, E. 2000, *MNRAS*, 314, 753
- Galli D., & Palla, F. 1998, *A&A*, 335, 403
- Gao, L., Theuns, T., Frenk, C. S., et al. 2010, *MNRAS*, 403, 1283
- Greif, T. H., Glover, S. C. O., Bromm, V., & Klessen, R. S. 2010, *ApJ*, 716, 510
- Hanawa, T., & Matsumoto, T. 2000, *PASJ*, 52, 241
- Hosokawa, T., Omukai, K., Yoshida, N., & Yorke, H. W. 2011, *Science*, 334, 1250
- Iocco, F., Mangano, G., Miele, G., Pisanti, O., & Serpico, P. D. 2009, *Phys. Rep.*, 472, 1
- Iwasaki, K., & Tsuribe, T. 2008, *PASJ*, 60, 125
- Iwasaki, K., Inutsuka, S. i., & Tsuribe, T. 2011a, *ApJ*, 733, 17
- Iwasaki, K., Inutsuka, S. i., & Tsuribe, T. 2011b, *ApJ*, 733, 16
- Kitayama, T., Yoshida, N., Susa, H., Umemura, M. 2004, *ApJ*, 613, 631
- Kitayama, T., & Yoshida, N. 2005, *ApJ*, 630, 675
- Lai, D. 2000, *ApJ*, 540, 946
- Larson, D., Dunkley, J., Hinshaw, G., et al. 2011, *ApJS*, 192, 16
- Larson, R. B. 1969, *MNRAS*, 145, 271
- Lipovka, A., Nunez-Lopez, R., & Avila-Reese, V. 2005, *MNRAS*, 361, 850
- Love, S. G., Joswiak, D. J., & Brownlee, D. E. 1994, *Icarus*, 111, 227
- Machida, M. N., Tomisaka, K., Nakamura, F., & Fujimoto, M. Y. 2005, *ApJ*, 622, 39
- Nagakura, T., Hosokawa, T., & Omukai, K. 2009, *MNRAS*, 399, 2183
- Omukai, K. 2000, *ApJ*, 534, 809
- Omukai, K., & Yoshii, Y. 2003, *ApJ*, 599, 746
- Omukai, K., Tsuribe, T., Schneider, R., & Ferrara, A. 2005, *ApJ*, 626, 627
- Omukai, K., & Nishi, R. 1998, *ApJ*, 508, 141
- Omukai, K., Hosokawa, T., & Yoshida, N. 2010, *ApJ*, 722, 1793
- Ostriker, J. P., & McKee, C. F. 1988, *Reviews of Modern Physics*, 60, 1
- Pollack, J. B., Hollenbach, D., Beckwith, S., et al. 1994, *ApJ*, 421, 615
- Portegies Zwart, S. F., McMillan, S. L. W., & Gieles, M. 2010, *ARA&A*, 48, 431
- Santoro, F., & Shull, J. M. 2006, *ApJ*, 643, 26
- Spitzer, L., Jr. 1978, *JRASC*, 72, 349
- Schneider, R., Ferrara, A., Salvaterra, R., Omukai, K., & Bromm, V. 2003, *Nature*, 422, 869
- Schneider, R., Omukai, K., Bianchi, S., & Valiante, R. 2012, *MNRAS*, 419, 1566
- Sedov, L. I. 1958, *Reviews of Modern Physics*, 30, 1077
- Shu, F. H., Lizano, S., Galli, D., Cantó, J., & Laughlin, G. 2002, *ApJ*, 580, 969
- Stahler, S. W., & Palla, F. 2005, *The Formation of Stars*, by Steven W. Stahler, Francesco Palla, pp. 865. ISBN 3-527-40559-3. Wiley-VCH, January 2005.,
- Sutherland, R. S., & Dopita, M. A. 1993, *ApJS*, 88, 253
- Tsuribe, T., & Omukai, K. 2008, *ApJ*, 676, L45
- Tumlinson, J. 2010, *ApJ*, 708, 1398
- Whalen, D., Abel, T., & Norman, M. L. 2004, *ApJ*, 610, 14
- Whalen, D., van Veelen, B., O'Shea, B. W., & Norman, M. L. 2008, *ApJ*, 682, 49
- Wang, H., Mo, H. J., Jing, Y. P., Yang, X., & Wang, Y. 2011, *MNRAS*, 413, 1973
- Whalen, D., Hueckstaedt, R. M., & McConkie, T. O. 2010, *ApJ*, 712, 101
- Yoshida, N., Abel, T., Hernquist, L., Sugiyama, N. 2003, *ApJ*, 592, 645
- Yoshida, N., Omukai, K., Hernquist, L., & Abel, T. 2006, *ApJ*, 652, 6
- Yoshida, N., Omukai, K., Hernquist, L. 2008, *Science*, 321, 669